Article

Electrochemical loading enhances deuterium fusion rates in a metal target

https://doi.org/10.1038/s41586-025-09042-7

Received: 6 September 2024

Accepted: 17 April 2025

Published online: 20 August 2025

Open access

Check for updates

Kuo-Yi Chen[1], Jannis Maiwald[1], Phil A. Schauer[1], Sergey Issinski[1], Fatima H. Garcia[1], Ryan Oldford[1], Luca Egoriti[2], Shota Higashino[1], Aref E. Vakili[1], Yunzhou Wen[1], Joseph Z. X. Koh[1], Thomas Schenkel[3], Monika Stolar[1], Amanda K. Brown[1] & Curtis P. Berlinguette[1,4,5,6] ✉

Nuclear fusion research for energy applications aims to create conditions that release more energy than required to initiate the fusion process[1]. To generate meaningful amounts of energy, fuels such as deuterium need to be spatially confined to increase the collision probability of particles[2–4]. We therefore set out to investigate whether electrochemically loading a metal lattice with deuterium fuel could increase the probability of nuclear fusion events. Here we report a benchtop fusion reactor that enabled us to bombard a palladium metal target with deuterium ions. These deuterium ions undergo deuterium–deuterium fusion reactions within the palladium metal. We showed that the in situ electrochemical loading of deuterium into the palladium target resulted in a 15(2)% increase in deuterium–deuterium fusion rates. This experiment shows how the electrochemical loading of a metal target at the electronvolt energy scale can affect nuclear reactions at the megaelectronvolt energy scale.

The Lawson criterion states that fusion reaction rates are governed by the density of the fuel, as well as time and temperature[1,5]. A higher density of fuel (for example, deuterium) increases the probability of particle collisions[1]. Magnetic and inertial confinement fusion, which are being widely studied for energy applications, typically achieve fuel densities of approximately 10^{20} m^{-3} and 10^{31} m^{-3}, respectively, for which the latter density exists for only hundreds of picoseconds[3,4,6]. It is, therefore, notable that a deuterium fuel density of 10^{28} m^{-3} can be easily achieved in a solid metal lattice[6] (Supplementary Note 1).

In 1934, Oliphant and Rutherford conducted the first demonstration of D–D nuclear fusion, during which they bombarded a target of solid metal, plated with deuterated material, with high-energy deuterium ions[7]. The incident deuterium ions (D^+) collided with deuterium embedded in the target. Fusion reactions using liquid[8], gas[9] and plasma[10] targets have since been demonstrated. For fusion reactions using solid-state targets, high-energy deuterium ions can be produced through accelerators[11], high-energy lasers[12,13] or gamma rays[14], each relying on a unique acceleration mechanism. Subsequently, the D^+ can collide with a deuterium atom (D) in the metal lattice to induce a D–D fusion event. Fusion rates within deuterated metals have been observed to surpass rates with gaseous targets[11,15].

In 1989, Fleischmann and Pons famously claimed that anomalous heat was generated during the electrolysis of deuterium oxide using a palladium cathode[16]. The anomalous heat was attributed to the nuclear fusion of D^+ drawn into the palladium lattice during electrolysis. Although this result could not be independently validated and was quickly dismissed[17–20], we were intrigued by the possibility of using electrochemistry at the eV energy scale to influence nuclear fusion reactions at the MeV energy scale[21]. To unambiguously validate such an effect, we took the position that we would need to measure nuclear signatures (for example, neutrons) rather than excess heat.

Building on these previous experimental observations, we set out to independently load a metal target with high concentrations of deuterium fuel to increase the probability of D–D fusion events within the target. To achieve this objective, we designed and built a benchtop particle accelerator, the 'Thunderbird Reactor', to: (1) deliver D^+ into a palladium target (by plasma immersion ion implantation, PIII (refs. 22,23)) to mediate D–D fusion events within the palladium metal lattice; and (2) electrochemically load the palladium target with deuterium sourced from $D_2O_{(l)}$ in an adjacent aqueous electrochemical cell[24–27]. The reactor is capable of detecting and quantifying neutrons formed during D–D fusion events that occur within the rigid palladium metal target that physically separates a vacuum chamber from the aqueous electrochemical cell.

The Thunderbird Reactor delivers D^+ sourced from a 'plasma thruster' (vide infra) through the vacuum chamber towards the palladium target. A dedicated power supply with an applied voltage ('sheath voltage') selectively accelerates the D^+ into the target. As the beam of incident D^+ loads deuterium into the palladium target ('phase I'), the rate of neutron production increases for a period of time, before reaching a constant rate. This experiment represents the first demonstration of PIII-induced D–D fusion. We also demonstrate that, while maintaining an incident beam of D^+ on the palladium, electrochemically loading the palladium target with deuterium from the adjacent electrochemical cell ('phase II') further enhances D–D fusion events by more than 10%. This experiment provides direct evidence that the electrochemical loading of a metal target at the eV energy scale can increase nuclear fusion rates at the MeV energy scale.

[1]Department of Chemistry, The University of British Columbia, Vancouver, British Columbia, Canada. [2]TRIUMF, Vancouver, British Columbia, Canada. [3]Accelerator Technology and Applied Physics Division, Lawrence Berkeley National Laboratory, Berkeley, CA, USA. [4]Department of Chemical and Biological Engineering, The University of British Columbia, Vancouver, British Columbia, Canada. [5]Stewart Blusson Quantum Matter Institute, The University of British Columbia, Vancouver, British Columbia, Canada. [6]Canadian Institute for Advanced Research (CIFAR), Toronto, Ontario, Canada. ✉e-mail: cberling@chem.ubc.ca

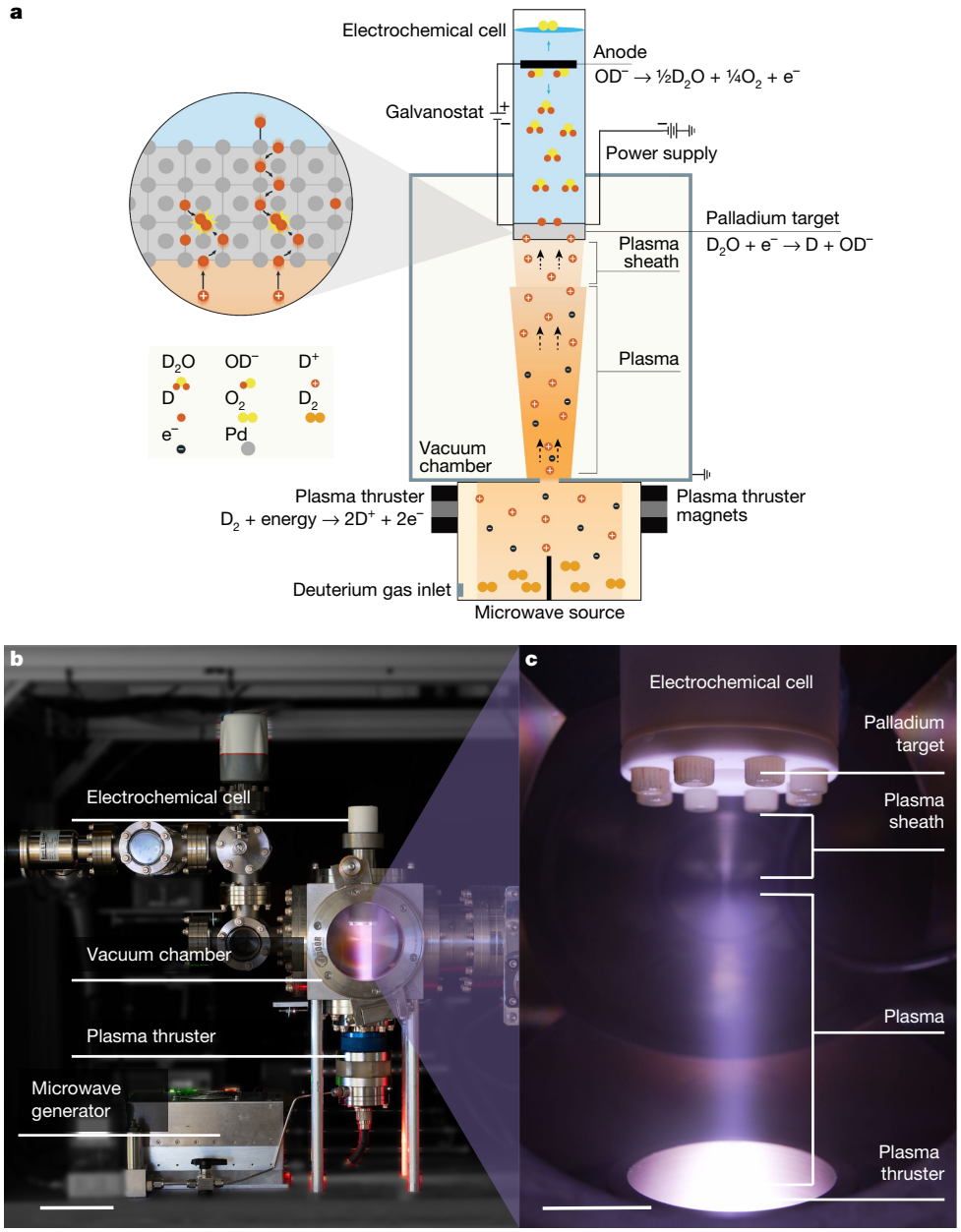

Fig. 1 | The Thunderbird Reactor. a, Working principle of the Thunderbird Reactor. Deuterium gas (D_2) is fed to the plasma thruster through the deuterium gas inlet. The D_2 is ionized by a microwave source. Plasma thruster magnets expel the resultant plasma of D^+ and e^- into the vacuum chamber. A −30-kV voltage applied across the palladium target and the vacuum chamber creates a plasma sheath enriched in D^+ and accelerates the D^+ into the palladium target, where nuclear fusion can occur. On the opposite side of the palladium target is an electrochemical cell that oxidizes OD^- into D_2O and $O_{2(g)}$ at the anode. The D_2O is reduced to D at the palladium target, which acts as a cathode. The D is then absorbed into the palladium target to potentially fuse with D sourced from the plasma thruster. The plasma current is set at 0.5 mA by the power supply and a galvanostat maintains a constant current of 200 mA across the anode and cathode of the electrochemical cell. **b**,**c**, Photographs of the Thunderbird Reactor (**b**) and the electrochemical cell (**c**). Scale bars, 10 cm (**b**); 2.5 cm (**c**).

The Thunderbird Reactor

The Thunderbird Reactor (Fig. 1) is a bespoke benchtop-sized particle accelerator designed and built to achieve electrochemically enhanced D–D nuclear fusion. The three main components of the reactor are a plasma thruster, a vacuum chamber and an electrochemical cell. We designed the reactor to be capable of plasma ion implantation to drive D^+ into a metal target to produce fusion reactions within the metal lattice. We selected a 300-µm-thick palladium target because palladium is capable of hosting high concentrations of deuterium[21]. The D^+ are generated in a custom-made plasma thruster driven by a 2.45-GHz microwave generator[28,29] and passed into a vacuum chamber by a set of axial ring magnets[30]. Within the vacuum chamber, set at 10^{-5} torr, the mean free path of electrons and D^+ greatly exceeded the dimensions of the chamber (Supplementary Note 2 and Supplementary Fig. 1). The plasma jet therefore traveled unobstructed from the plasma thruster to the palladium target. A high negative voltage applied to the palladium target repels electrons and created a 'plasma sheath' close to the target. This plasma sheath was enriched in D^+ and was visible to the naked eye (Fig. 1). A power supply created a sheath voltage to accelerate the D^+ entering the sheath to keV energies and implant them in the target (Fig. 1). Note that this design does not require complex ion optics and accelerating grids. Thus, the footprint of the Thunderbird Reactor is only 120 × 80 × 70 cm^3 and fits on a standard laboratory bench.

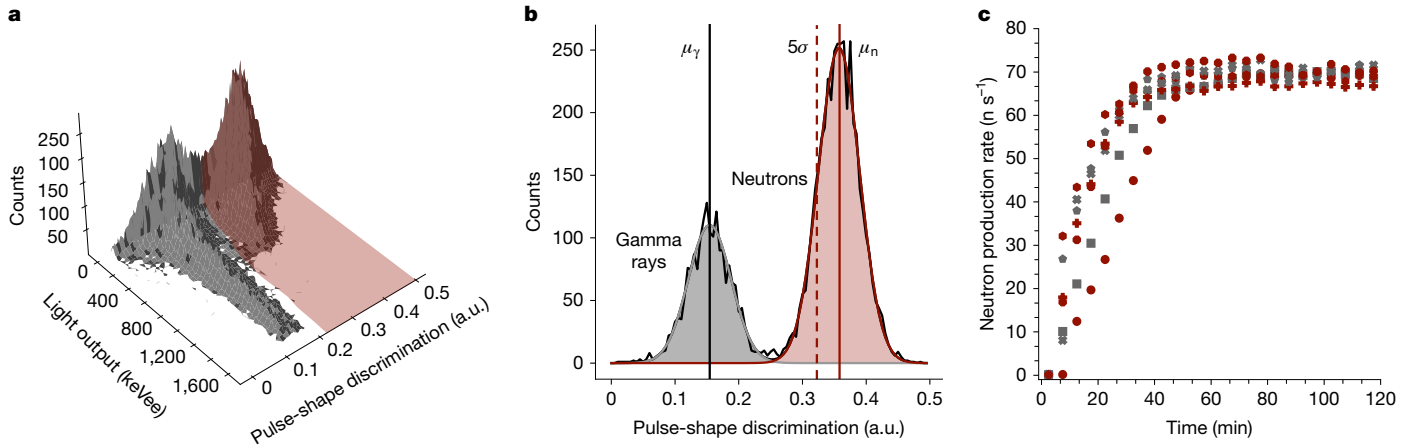

Fig. 2 | Neutron diagnostics and discrimination. a, The 3D distribution showing the neutron counting window (red). The red region shows the particles that are identified as neutrons, separate from the gamma-ray distribution. **b**, A sample slice of the 3D distribution taken at 195 keVee with a width of 15 keVee. The solid (black and red) lines are the mean (μ_γ and μ_n) of the gamma-ray (grey area) and neutron (red area) distributions, respectively, each with a standard deviation of σ. The dashed (red) line delineates the gamma-ray window, placed at $\mu + 5\sigma$; more than 99.9999% of all gamma rays are contained in the region to the left of this line. Those particles found to the right of this line are classified as neutrons. **c**, The results of seven independent beam-loading experiments at −30 kV and 0.2 mA using different palladium targets show that neutron production rates are approximately the same 69.3(2) n s^{-1} after 120 min of reactor operation. a.u., arbitrary units.

The reactor was operated using custom-built software and interface (Supplementary Note 3).

On the opposite side of the palladium target, an electrochemical cell contained 2 M $K_2CO_{3(aq)}$ in D_2O. The D_2O was reduced at the palladium target into D and OD^- (equation (1)). The oxidation of OD^- at an iridium anode formed D_2O and $O_{2(g)}$ (ref. 31) (equation (2)). The electrochemically reduced D atoms were absorbed into the palladium lattice with a Faradaic efficiency of 51% (Supplementary Note 4 and Supplementary Fig. 2). The electrochemical cell was inspired by our previous work on palladium membrane reactors and modified to function within the vacuum chamber (Supplementary Note 5 and Supplementary Fig. 3). Note that $D_{2(g)}$ could form on either face of the palladium during electrolysis. The palladium therefore served as the cathode and membrane for the electrochemical cell, a target for D^+ sourced from the plasma thruster, and a physical separator between the vacuum and the electrochemical cell.

$$\text{Cathode reaction}: D_2O + e^- \rightarrow D + OD^- \quad (1)$$

$$\text{Anode reaction}: OD^- \rightarrow \frac{1}{2}D_2O + \frac{1}{4}O_2 + e^- \quad (2)$$

The fusion of two deuterium atoms is expected to produce, with equal probability, (1) a neutron (n) and helium-3 (^{3}He) with kinetic energies of 2.45 MeV and 0.82 MeV, respectively (equation (3)) or (2) a proton (^{1}H) and tritium (^{3}H) with kinetic energies of 3.02 MeV and 1.01 MeV, respectively (equation (4)). A third possible reaction is the production of ^{4}He and a gamma ray[32,33] (γ) with an energy of 23.8 MeV (equation (5)), but there is a low probability (10^{-5}%) of this reaction occurring[34] and it is not considered here.

$$D + D \rightarrow {}^3He + n^0 \quad (3)$$

$$D + D \rightarrow {}^3H + {}^1H \quad (4)$$

$$D + D \rightarrow {}^4He + \gamma \quad (5)$$

To test whether nuclear fusion rates could be enhanced on electrochemical loading of the palladium target, we measured neutrons as a proxy for fusion events. Because the walls of the vacuum chamber are effectively transparent to 2.45-MeV neutrons, we used a neutron-sensitive scintillation detector coupled with a photomultiplier tube[35,36], positioned 12 cm from the palladium target. This detector was located outside the vacuum chamber for protection from the harsh environment within the reactor. The detection system enabled the differentiation of neutrons from background gamma rays using pulse-shape discrimination of the digitized detector signals (Fig. 2, Supplementary Note 6 and Supplementary Figs. 4–7). Consequently, we were able to exclude more than 99.9999% of gamma rays.

Nuclear fusion by PIII

To validate fusion events in the Thunderbird Reactor, we first performed a control experiment in each experimental campaign. Before turning on the reactor for any experiment, we would collect 5 min of background neutron measurements. This background neutron production rate was measured to be 0.21(9) neutrons per second (n s^{-1}) in our laboratory environment and we observed a constant rate of background neutrons over a 24-h period (Supplementary Fig. 8). For all of our experiments, including the control experiment, we fed $D_{2(g)}$ into the thruster at a rate of 0.5 sccm and turned on the plasma thruster by using a 200-W burst of microwave power over 5 s to initiate the ionization process. We then applied 15 W to sustain the operation. The plasma current was held at 0.5 mA to control for neutron yield. The target became engulfed in plasma (Fig. 1). The high voltage (−30 kV) across the target and vacuum chamber, defined herein as the 'sheath voltage', would then repel negative charge from the palladium to create a plasma sheath. The D^+ within the plasma sheath were accelerated to an energy of 30 keV to bombard the target and induce D–D fusion. The modelled penetration depth of the D^+ into the palladium lattice was 0.18 µm from the surface of the palladium target facing the ion beam (Supplementary Note 7 and Supplementary Fig. 9).

After activating the plasma thruster and applying the sheath voltage, the neutron production rate increased from the background value of 0.21(9) n s^{-1} to a stable value of 130–140 n s^{-1} after approximately 30 min (Fig. 3). We defined the neutron production rate to be stable when it remained within ±5% of its mean value over a 30-min period after the sheath voltage was applied. The measured neutron energy was consistent with that expected from D–D fusion reactions. To validate our results, we first benchmarked the measured neutron response

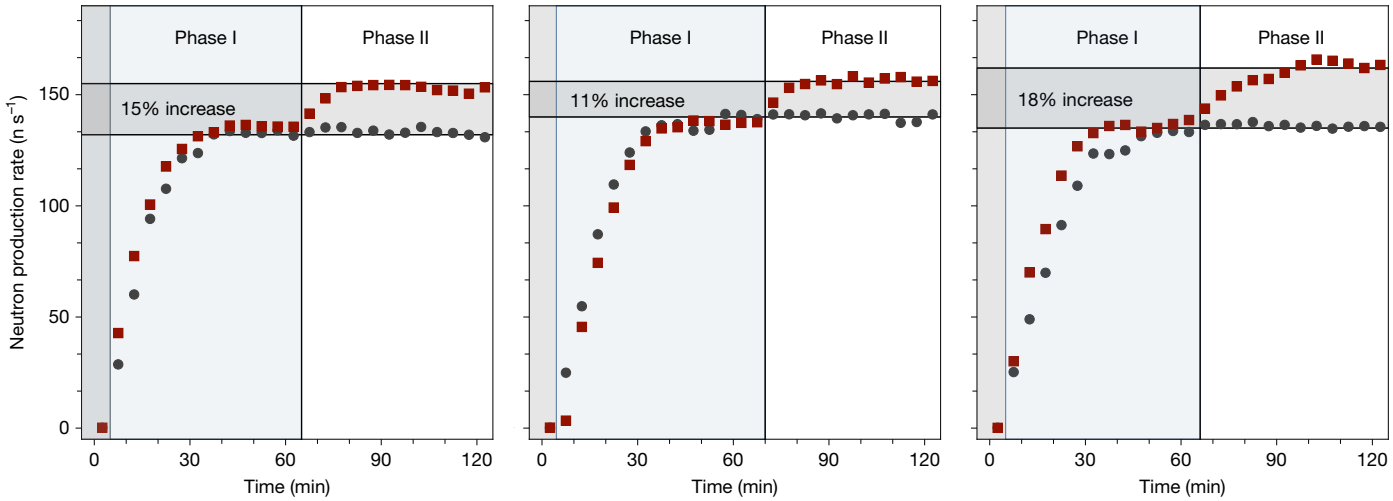

Fig. 3 | Neutron production rates in the Thunderbird Reactor. Three separate experimental campaigns showing neutron production rate using PIII as a function of time, with and without electrochemical loading of the palladium target. Each campaign was performed by first using PIII on the target for 2 h (grey circles). The palladium target was removed from the reactor, placed under vacuum at 400 °C for 1 h to remove the loaded deuterium and then reinserted into the reactor (Supplementary Information). The same PIII procedure was repeated. After the rate of neutron production reached a constant value, the electrochemical cell was turned on to load palladium with further D sourced from $D_2O_{(l)}$ (red squares). Note that phase I (beam loading only) of the successive experiments produces similar neutron production rate profiles. The neutron production rates increase by 15.1(1)%, 11.3(1)% and 18.5(2)% with electrochemical loading (phase II; red squares) for the three experimental campaigns shown here. The grey area before phase I represents collection of the background neutron production rate before turning on the plasma thruster.

against simulations from two Monte Carlo transport codes: MCNP 6.2 (ref. 37) (used in conjunction with the detector response function toolkit DRiFT[38]) and Geant4 (refs. 39–41). The simulated results from both codes were in good agreement with each other and also with the experimental response. We then unfolded the measured neutron response using the GRAVEL algorithm[42] and a detector response matrix simulated with Geant4 (Supplementary Note 6 and Supplementary Fig. 7). The unfolded spectrum from the Thunderbird Reactor closely matched the spectrum from simulated D–D fusion response in Geant4, providing further evidence for the D–D fusion origin of the detected neutrons.

The initial increase and eventual saturation of the neutron production rate during the beam-loading experiment was consistent with fusion occurring within the lattice of the metal target and not within the gas or plasma phase (Supplementary Note 8 and Extended Data Fig. 1).

Electrochemically enhanced fusion

The next stage of our experiments was to test whether the electrochemical loading of the palladium target would increase the neutron production rates. To test for this effect, after the control experiment we removed the target from the reactor and annealed the target at 400 °C for 1 h at 10^{-5} torr to remove deuterium from the metal[43]. X-ray diffraction (XRD) characterization of the palladium target, before and after annealing, confirmed that the annealing successfully removed deuterium from the palladium lattice (Supplementary Fig. 10). We reinserted the palladium target in the reactor and repeated the same procedure described above for the control experiment. If the neutron production rate profiles matched the control experiment, we would move on to the next stage of electrochemically loading the palladium target. After the reactor reached a stable neutron production rate (usually after 60 min), the adjacent electrochemical cell was turned on. A total current of 200 mA was applied across the anode and cathode and was kept constant by using the power supply in galvanostatic mode. Deuterium levels in the vacuum chamber, which were detected by a residual gas analyser, started to increase 2 min after turning on the electrochemical cell. This increase is consistent with deuterium being passed through the palladium target with electrochemical loading. Independent in situ XRD characterization of the palladium target revealed that the electrochemical current successfully loaded the palladium target with a high concentration of deuterium (D/Pd molar ratio of 0.7), which remained in the palladium lattice under ambient conditions (Supplementary Figs. 11 and 12 and Extended Data Figs. 3–6).

The most important aspect of this study is that we observed an increase in neutron production rate after the electrochemical cell was turned on. As shown in Fig. 3, the neutron production rates increased from phase I saturation of 135.5(5), 142.9(5) and 138.6(3) n s^{-1} for three separate targets to a new saturation in phase II of 156.7(4), 159.2(5) and 164.3(13) n s^{-1}, respectively, representing an average increase of 15(2)% in neutron production rate owing to electrochemical loading. We suggest that the difference in the neutron production rate between each experiment during electrochemical loading arises from H_2O contamination in the deuterated electrolyte with exposure to the ambient atmosphere over time (Supplementary Note 9 and Supplementary Fig. 13). An independent experiment using 2 M K_2CO_3 in H_2O as the electrolyte showed a large reduction in neutron production rate (decrease of 88.3(3)%; Extended Data Fig. 2).

When the electrochemical cell was turned off, neutron production rates varied by no more than 2% compared with the maximum observed during the 'on' period (Extended Data Fig. 7). This is because the fraction of D atoms that undergo fusion is much lower than that in the electrochemically loaded palladium target (Supplementary Note 10). We independently confirmed, using in situ XRD methods, that the deuterium that is electrochemically loaded into the target does not exit the palladium membrane on a timescale relevant to the experiment under ambient conditions or under vacuum (Extended Data Figs. 5 and 6). When the electrochemical cell was turned back on, the neutron production rate increased yet again but to a lesser extent (6% increase) than the 20% increase in the initial cycle (Extended Data Fig. 7).

The reduction of D_2O when using the palladium target as a cathode increases the concentration of D atoms in the palladium lattice to

form a stoichiometric ratio that matches approximately $PdH_{0.7}$ (ref. 27) (Supplementary Figs. 11 and 12 and Extended Data Figs. 3–6). In the Thunderbird Reactor, we assume the D/Pd ratio to be approximately the same. Although we were unable to directly measure the D/Pd ratio during the fusion experiment, we can claim that some amount of D being electrochemically adsorbed into the palladium target increases the rate of nuclear fusion. This claim is supported by the fact that we did not observe an increase in the rate of nuclear fusion when H_2O, instead of D_2O, was used in the electrochemical chamber (Extended Data Fig. 2). Future experiments will seek to define the exact ratio of D atoms at or near the surface of the palladium target to more clearly define how nuclear fusion rates are correlated to D concentrations in the palladium lattice.

Conclusion

We built the Thunderbird Reactor to bridge chemical reactions and nuclear reactions that occur at the eV and MeV energy scales, respectively. Using the Thunderbird Reactor, we demonstrated that the electrochemical loading of a metal target can increase D–D fusion rates, driven by PIII, by an average of 15(2)%. This slight increase in neutron production rate is constrained by the maximum D/Pd ratio of 1 at room temperature, unless other unknown mechanisms contribute to the fusion gain. Although this represents the first incontrovertible example of electrochemistry increasing target fuel density and, in turn, nuclear fusion rates[16,21], the Thunderbird Reactor produces a neutron yield equivalent to only 10^{-9} W with 15 W of input power (Supplementary Note 11). Many more advances are needed for the Thunderbird Reactor to achieve net energy gain, wherein the fusion reactions produce more energy than consumed.

There are many ways in which the nuclear fusion, materials science and electrochemistry communities can increase this power output. For example, the deuterium fuel densities within the metal target can be increased by either using an inductively coupled plasma that can be maintained at higher pressures to make more ions available at the target[44] or using metals capable of higher deuterium loadings (for example, Nb, Ti)[45]. It is also intriguing whether ^{3}He and tritium, produced by D–D fusion, could fuel secondary fusion reactions in the target within a deuterium-rich (PdD) environment. There is also an opportunity to make use of quantum coherence effects with target materials and with coherent stimuli[46,47]. This reactor could also help answer fundamental questions related to screening effects and intranuclear resonances at lower energies (<5 keV)[21,48,49]. The ability to influence the target within an accessible benchtop-scale fusion reactor, which is also coupled to an adjacent electrochemical cell capable of controlling local and transient fuel density, presents many new avenues of exploration for advancing the nuclear fusion sciences.

Online content

Any methods, additional references, Nature Portfolio reporting summaries, source data, extended data, supplementary information, acknowledgements, peer review information; details of author contributions and competing interests; and statements of data and code availability are available at https://doi.org/10.1038/s41586-025-09042-7.

1. Lawson, J. D. Some criteria for a power producing thermonuclear reactor. *Proc. Phys. Soc. B* **70**, 6 (1957).
2. Kawarasaki, Y. Possible in-lattice confinement fusion (LCF). *AIP Conf. Proc.* **369**, 1244–1249 (1996).
3. Hurricane, O. A. et al. Fuel gain exceeding unity in an inertially confined fusion implosion. *Nature* **506**, 343–348 (2014).
4. Osolin, C. Nuclear diagnostics help pave way to ignition on NIF. *Lawrence Livermore National Laboratory* https://www.llnl.gov/article/46181/nuclear-diagnostics-help-pave-way-ignition-nif#:~:text=At%20its%20peak%2C%20a%20NIF,100%20trillionths%20of%20a%20second (2020).
5. Wurzel, S. E. & Hsu, S. C. Progress toward fusion energy breakeven and gain as measured against the Lawson criterion. *Phys. Plasmas* **29**, 062103 (2022).
6. Kawarasaki, Y. Possible In-lattice Confinement Fusion (LCF): dynamic application of atomic and nuclear data. In *Proc. 1994 Symposium on Nuclear Data* (eds Kawai, M. & Fukahori, T.) 258–261 (Japan Atomic Energy Research Institute, 1995).
7. Oliphant, M. L. E., Harteck, P. & Rutherford, L. Transmutation effects observed with heavy hydrogen. *Proc. R. Soc. Lond. A Math. Phys. Sci.* **144**, 692–703 (1934).
8. Ke, J. et al. A compact accelerator-driven deuterium–deuterium neutron source using heavy water jet target. *Nucl. Instrum. Methods Phys. Res. A* **997**, 165165 (2021).
9. Deluca, P. M. et al. Performance of a gas target neutron source for radiotherapy. *Phys. Med. Biol.* **23**, 876–887 (1978).
10. Lang, R. F. et al. Characterization of a deuterium–deuterium plasma fusion neutron generator. *Nucl. Instrum. Methods Phys. Res. A* **879**, 31–38 (2018).
11. Raiola, F. et al. Electron screening in d(d,p)t for deuterated metals and the periodic table. *Phys. Lett. B* **547**, 193–199 (2002).
12. Torrisi, L., Cavallaro, S., Cutroneo, M., Krasa, J. & Klir, D. D–D nuclear fusion induced by laser-generated plasma at 10^{16} W cm^{-2} intensity. *Phys. Scr.* **2014**, 014026 (2014).
13. Kautz, E. J., Senor, D. J. & Harilal, S. S. The interplay between laser focusing conditions, expansion dynamics, ablation mechanisms, and emission intensity in ultrafast laser-produced plasmas. *J. Appl. Phys.* **130**, 204901 (2021).
14. Steinetz, B. M., Benyo, T. L., Chait, A. & Hendricks, R. C. Novel nuclear reactions observed in Bremsstrahlung-irradiated deuterated metals. *Phys. Rev. C* **101**, 044610 (2020).
15. Raiola, F. et al. Enhanced electron screening in d(d,p)t for deuterated metals. *Eur. Phys. J. A* **19**, 283–287 (2004).
16. Fleischmann, M. & Pons, S. Electrochemically induced nuclear fusion of deuterium. *J. Electroanal. Chem. Interfacial Electrochem.* **261**, 301–308 (1989).
17. Miskelly, G. M. et al. Analysis of the published calorimetric evidence for electrochemical fusion of deuterium in palladium. *Science* **246**, 793–796 (1989).
18. Albagli, D. et al. Measurement and analysis of neutron and gamma-ray emission rates, other fusion products, and power in electrochemical cells having Pd cathodes. *J. Fusion Energy* **9**, 133–148 (1990).
19. Williams, D. E. et al. Upper bounds on 'cold fusion' in electrolytic cells. *Nature* **342**, 375–384 (1989).
20. Maddox, J. Farewell (not found) to cold fusion. *Nature* **344**, 365–366 (1990).
21. Berlinguette, C. P. et al. Revisiting the cold case of cold fusion. *Nature* **570**, 45–51 (2019).
22. Conrad, J. R., Radtke, J. L., Dodd, R. A., Worzala, F. J. & Tran, N. C. Plasma source ion-implantation technique for surface modification of materials. *J. Appl. Phys.* **62**, 4591–4596 (1987).
23. Conrad, J. R., Dodd, R. A., Worzala, F. J. & Qiu, X. Plasma source ion implantation: a new, cost-effective, non-line-of-sight technique for ion implantation of materials. *Surf. Coat. Technol.* **36**, 927–937 (1988).
24. Sherbo, R. S., Delima, R. S., Chiykowski, V. A., MacLeod, B. P. & Berlinguette, C. P. Complete electron economy by pairing electrolysis with hydrogenation. *Nat. Catal.* **1**, 501–507 (2018).
25. Itoh, N. & Xu, W.-C. Selective hydrogenation of phenol to cyclohexanone using palladium-based membranes as catalysts. *Appl. Catal. A* **107**, 83–100 (1993).
26. Kurimoto, A., Sherbo, R. S., Cao, Y., Loo, N. W. X. & Berlinguette, C. P. Electrolytic deuteration of unsaturated bonds without using D_2. *Nat. Catal.* **3**, 719–726 (2020).
27. Benck, J. D., Jackson, A., Young, D., Rettenwander, D. & Chiang, Y.-M. Producing high concentrations of hydrogen in palladium via electrochemical insertion from aqueous and solid electrolytes. *Chem. Mater.* **31**, 4234–4245 (2019).
28. Chen, K.-Y. & Zhong, B.-J. Compact permanent magnet hexapole ECR ion thruster. In *2022 IEEE Aerospace Conference (AERO)* (IEEE, 2022).
29. Chen, K.-Y. & Zhong, B.-J. Design of compact hexapole ECR ion thruster. In *AIAA AVIATION 2022 Forum* (AIAA, 2022).
30. Chen, K.-Y. & Zhong, B.-J. Electron trajectory simulation in compact hexapole ECR ion thruster. In *AIAA AVIATION 2022 Forum* (AIAA, 2022).
31. Rojas, J. et al. Technoeconomics and carbon footprint of hydrogen production. *Int. J. Hydrogen Energy* **49**, 59–74 (2024).
32. Woods, L. C. *Theory of Tokamak Transport: New Aspects for Nuclear Fusion Reactor Design* (Wiley, 2005).
33. Dolan, T. J. *Fusion Research: Principles Experiments and Technology* (Pergamon Press, 2000).
34. Cecil, F. E., Cole, D. M., Wilkinson, F. J. III & Medley, S. S. Measurement and application of DDγ, DTγ and D3Heγ reactions at low energy. *Nucl. Instrum. Methods Phys. Res. B* **10-11**, 411–414 (1985).
35. Eljen Technology. Neutron/gamma PSD liquid scintillator EJ-301, EJ-309. *Eljen Technology* https://eljentechnology.com/images/products/data_sheets/EJ-301_EJ-309.pdf (2021).
36. Paff, M. G., Clarke, S. D. & Pozzi, S. A. Organic liquid scintillation detector shape and volume impact on radiation portal monitors. *Nucl. Instrum. Methods Phys. Res. A* **825**, 31–39 (2016).
37. Armstrong, J. et al. MCNP user's manual, LA-UR-17-29981. *Los Alamos National Laboratory* https://mcnp.lanl.gov/pdf_files/TechReport_2017_LANL_LA-UR-17-29981_WernerArmstrongEtAl.pdf (2017).
38. Andrews, M. T., Bates, C. R., Pinilla, M. I., McKigney, E. A. & Sood, A. Development of validated detector models with MCNP® and DRiFT. In *2017 IEEE Nuclear Science Symposium and Medical Imaging Conference (NSS/MIC)* 1–3 (IEEE, 2017).
39. Allison, J. et al. Recent developments in Geant4. *Nucl. Instrum. Methods Phys. Res. A* **835**, 186–225 (2016).
40. Allison, J. et al. Geant4 developments and applications. *IEEE Trans. Nucl. Sci.* **53**, 270–278 (2006).
41. Agostinelli, S. et al. Geant4—a simulation toolkit. *Nucl. Instrum. Methods Phys. Res. A* **506**, 250–303 (2003).
42. Hao, C. Y. et al. Unfolding the fast neutron spectra of a BC501A liquid scintillation detector using GRAVEL method. *Sci. China Phys. Mech. Astron.* **57**, 1885–1890 (2014).
43. Holleck, G. L. Diffusion and solubility of hydrogen in palladium and palladium–silver alloys. *J. Phys. Chem.* **74**, 503–511 (1970).

44. Kazakov, Y. O. et al. Efficient generation of energetic ions in multi-ion plasmas by radio-frequency heating. *Nat. Phys.* **13**, 973–978 (2017).
45. Santucci, A., Tosti, S. & Basile, A. in *Handbook of Membrane Reactors* (ed. Basile, A.) 183–217 (Woodhead Publishing, 2013).
46. Xi, Z., Li, Y. & Fan, H. Quantum coherence and correlations in quantum system. *Sci. Rep.* **5**, 10922 (2015).
47. Tan, K. C., Kwon, H., Park, C.-Y. & Jeong, H. Unified view of quantum correlations and quantum coherence. *Phys. Rev. A* **94**, 022329 (2016).
48. Czerski, K. Deuteron-deuteron nuclear reactions at extremely low energies. *Phys. Rev. C* **106**, L011601 (2022).
49. Casey, D. T. et al. Thermonuclear reactions probed at stellar-core conditions with laser-based inertial-confinement fusion. *Nat. Phys.* **13**, 1227–1231 (2017).

Methods

Materials

Potassium carbonate (K_2CO_3, 99%) was purchased from Thermo Fisher Scientific. K_2CO_3 was kept in a Napco 5831 vacuum oven at 120 °C for at least 24 h to eliminate the residual water. Deuterium oxide (D_2O, 99.9%) was purchased from Cambridge Isotope Laboratories and used as received. Iridium wire (0.5 mm, 99.95%) was obtained from Taobao. Ag/AgCl reference electrodes (CHI111) were purchased from CH Instruments. Potassium chloride saturated in H_2O was purchased from Fisher Chemical and used as received. Potassium hydroxide (KOH, ≥85%, pellets) was purchased from Sigma-Aldrich and used as a ^{40}K radioactive gamma-ray-emitting source during the neutron detector calibration process.

Plasma thruster

The plasma thruster is custom made from SS-316 stainless steel and includes three ring magnets and a set of hexapole magnets. A type N feedthrough, located below the plasma thruster, functions as an antenna to transmit microwaves into the plasma thruster (Supplementary Fig. 14). The type N feedthrough transmits the microwaves by means of a coaxial cable and is controlled through a proportional–integral–derivative (PID) loop. The deuterium flow rate is adjusted by a mass flow controller and fed into the gas inlet on the side of the thruster through SS-304 stainless-steel pipes. The detailed components of the plasma thruster, along with their make and model, are as follows: microwave antenna (Kurt J. Lesker, SS, IFTNG012033M, Type N Feedthrough), ring magnet (CMS Magnetics, NR011-42N, N42 neodymium), bar magnet (20 × 10 × 10 mm N35 neodymium), mass flow controller (ASERT, AST10-DLCMX) and microwave generator (Wattsine, WSPS-2450-200M).

Vacuum chamber

The vacuum chamber is a 6-inch 6-way standard ConFlat flange cube (Supplementary Fig. 15) used to provide an environment for the operation of the plasma thruster and PIII into the palladium target. The vacuum chamber physically connects the plasma thruster and the electrochemical cell together. The vacuum system consists of a turbo pump, two dry scroll pumps and a pressure gauge and can reach a minimum pressure of 5×10^{-8} torr. Furthermore, the vacuum system is equipped with a residual gas analyser to monitor the types of residual gas in the vacuum chamber. The vacuum chamber pressure is maintained between 1×10^{-5} and 2×10^{-5} torr during beam loading. The lowest pressure of the vacuum chamber during the electrochemical loading was approximately 4×10^{-5} torr. The detailed components of the vacuum chamber, along with their make and model, are as follows: dry scroll pump (Agilent, IDP-7), turbo pump (Agilent, TwisTorr 305 FS), pressure gauge (Edwards, WRG-S-DN40CF), turbo controller (Edwards, Turbo and Instrument Controller), residual gas analyser (SRS, RGA100), plasma thruster holder (Ideal Vacuum, SS, SWIFT-SEAL P1011088), manual gate valve (Kurt J. Lesker, SS, GV0400MVCF), pneumatic bellows sealed angle valve (Kurt J. Lesker, SS, SA0150PVCF) and vacuum chamber (Kurt J. Lesker, SS, CU6-0600, 6-inch CF UHV Cube).

Electrochemical cell

The housing of the electrolysis chamber was custom made from Macor (Machinable Glass Ceramic) and machined in-house using lathes and mills. A Viton O-ring holds the palladium target in place, physically separating the interface between the electrolyte and the vacuum. A brass rod, travelling the length of the electrochemical cell through a channel, connects the palladium target to the high-voltage power supply needed to drive fusion reactions (Supplementary Fig. 16). The detailed components of the electrolysis chamber, along with their make and model, are as follows: electrochemical cell holder (Taobao, SS, KF50 to 50 mm Compression port), spring probe (QA Technology, 100-PLN1609L), viton O-ring (McMaster-Carr, 1284N116), DC–DC converter (Walfront, Buck Boost ZK-4KX), lead-acid battery (Zeus, PC5-12F1-5), remote control switch (eMylo, R121A) and high-voltage power supply (JIAMAN, H2105N-30-17).

Because the target is held at a high negative voltage (−30 kV), the electrochemical reaction is driven by a floating galvanostat. The galvanostat consists of a DC–DC converter and is powered by a 12 V lead-acid battery. The galvanostat is set to drive the electrochemical reactions at 200 mA between the cathode and the anode for the electrochemical reaction (Supplementary Fig. 17).

As well as connecting the galvanostat, the brass rod is also connected to a negative high-voltage power supply to drive the fusion reaction. The current value recorded by the high-voltage power supply is returned to the PID system as feedback data for automatic control of the PIII current.

Fusion reactions in the Thunderbird Reactor

The annealed and cleaned palladium target was installed into the electrochemical cell, which was then installed into the vacuum chamber. Vacuum was applied to the vacuum chamber until a pressure of less than 5×10^{-6} torr was reached. Once a high vacuum was reached, deuterium gas was supplied to the plasma thruster at a flow rate of 0.5 sccm by a mass flow controller. The reactor control software was started after the mass flow controller read a steady flow rate of 0.5 sccm. The microwave generator was turned on with an input power of 10 W. The gate valve to the vacuum chamber was closed, and the vacuum decreased from 5×10^{-6} torr to 1×10^{-2} torr. We found that reduced vacuum conditions facilitate easier ignition of the plasma. The microwave generator power was increased to 200 W to ignite the plasma, which was verified visually by observing light at the reactor pinhole opening (Supplementary Fig. 18a). The gate valve was then opened to the vacuum chamber. The vacuum chamber pressure stabilized between 1×10^{-5} and 2×10^{-5} torr. The PIII thruster current was controlled through a PID loop (see the above 'Plasma thruster' section), which was set to 0.5 mA, with lower and upper thresholds of 0.3 and 0.6 mA, respectively.

The background rate of neutrons was collected for 5 min using the CAEN CoMPASS software[50]. The reactor was then started by applying −30 kV to the palladium target using a high-voltage power supply. When the high negative voltage is applied to a target immersed in plasma, electrons are repelled, generating a plasma sheath (Supplementary Fig. 18b). The plasma sheath, an electron-depleted region, appears darker than the plasma jet because it is difficult for ions to recombine with electrons. This sheath has a strong electrostatic field. As ions from the plasma jet enter this region, they are accelerated by the sheath voltage and implanted into the target. A 6.67-mm pinhole is placed at the exit of the plasma thruster during the experiment. The purpose of the pinhole is to limit the PIII current to the 0.5 mA set for the reactor conditions.

For a beam-loading experiment, the neutron production rate was collected for approximately 2 h. In a typical experiment, a stable state (when the rate of neutron production is no longer changing as a function of time) was reached after approximately 30 min. We define steady state as the period during which all data points remain within ±5% of their mean value over a 30-min interval following the application of high voltage.

For an electrochemically enhanced experiment, the procedure was the same as above except that the electrochemical cell was turned on after approximately 1 h of reactor operation (see the next section, 'Electrochemistry in the Thunderbird Reactor'). The electrochemical cell was operated until the stable state was observed after the initial increase in the rate of neutron counts. The vacuum chamber pressure increased over time during the operation of the electrochemical cell, and the final pressure was usually between 3.5×10^{-5} and 4×10^{-5} torr.

Electrochemistry in the Thunderbird Reactor

All electrochemistry in the Thunderbird Reactor was conducted galvanostatically at a total current of 200 mA. A combination of a 12 V battery

and a DC–DC converter was used to power the electrochemical cell. At a cell current of 200 mA, the cell voltage was approximately 3.8 V (Supplementary Fig. 19). The electrochemical cell was manufactured from a cylindrical piece of Macor (Machinable Glass Ceramic; see the above section, 'Electrochemical cell') with a diameter of 50 mm, a length of 265 mm and a 1-cm-diameter opening on the bottom facing the vacuum chamber. The palladium target, 300 μm in thickness with a geometric surface area of 1.5 cm^2 exposed to the electrolyte, served as the cathode. The palladium target was sealed with an O-ring at the bottom of the electrochemical cell, with a geometric surface area of 0.785 cm^2 exposed to the vacuum chamber. The preparation of palladium targets is described in the 'Palladium target/cathode preparation' section. The anode was an iridium wire, 320 mm in length and 0.5 mm in diameter. The iridium wire was rinsed with deionized water, dried with a Kimwipe and heated with a propane torch to eliminate adsorbed water. The cleaned iridium wire was placed into the electrochemical cell at a distance of 1 mm from the cathode. The electrochemical cell was filled with 17 g (13 ml) of 2 M K_2CO_3 in D_2O. The galvanostat was connected to the Pd target and the iridium wire using alligator clips to complete the electrochemical set-up.

Electrochemical cycling in the Thunderbird Reactor

The effect of power cycling of the electrochemical cell was tested by turning the galvanostat on and off. An electrochemically enhanced experiment was conducted as described above (see the 'Fusion reactions in the Thunderbird Reactor' and 'Electrochemistry in the Thunderbird Reactor' sections), with the electrochemical cell being activated after 60 min of beam loading and the neutron production rate stabilizing at 172.6(4) n s^{-1}. The electrochemical cell was then turned off and on, at intervals of 30 min, while the beam loading of the Pd target with plasma continued (Extended Data Fig. 7).

Palladium target/cathode preparation

The palladium target was rolled from a palladium bar (100 g, 99.95% purity, purchased from Valcambi). The bar was first manually cold-rolled to <500 μm using a Pepetools 90MM Flat Rolling Mill, then automatically cold-rolled to a final thickness of 300 μm using an MTI EQ-MR100A Electric Roller Press. The final thickness was measured with a Mitutoyo digital micrometer to an accuracy of ±1 μm. Targets were cut from the 300-μm palladium sheet into a disc shape with a diameter of 2.4 cm using a die cutter. The disc-shaped targets were cleaned with deionized water and annealed at 400 °C for 1 h at 10^{-5} torr in a 50-mm quartz vacuum tube installed in an MTI OTF-1200X-S tube furnace. After annealing, the targets were polished with sandpaper (CW 1200) and washed with isopropyl alcohol using a Kimwipe before use in the reactor. The annealing and cleaning procedures were performed between each fusion experiment to remove deuterium from the palladium. The targets were characterized with XRD to confirm the absence of deuterium from the palladium lattice.

The annealing procedure was based on Sieverts' law. According to Holleck[43], the relationship between the hydrogen concentration in metals and hydrogen gas pressure is given by:

$$\left(\frac{P_{H2}}{P_0}\right)^{1/2} = K(T)n$$

in which P_{H2} is the partial pressure of hydrogen, P_0 is 1 torr, $K(T)$ is Sieverts' constant at a specified temperature (for example, 2.1×10^3 at 400 °C) and n is the molar ratio of hydrogen in the metal.

We assumed the volume fraction of hydrogen gas in the vacuum chamber to be the same as that in ambient air, 5×10^{-5} vol% (ref. 51), which results in $P_{H2} = 5.0 \times 10^{-12}$ torr for the total pressure of 10^{-5} torr in the vacuum tube furnace. The molar ratio of hydrogen (n) at 400 °C is:

$$n = \left(\frac{5 \times 10^{-12}\,\text{torr}}{1\,\text{torr}}\right)^{1/2} \Big/ (2.1 \times 10^3) = 1.1 \times 10^{-9}$$

This low value of n suggests that the palladium targets will be completely deloaded of hydrogen atoms at a temperature of 400 °C. The deloading was validated experimentally using XRD (Supplementary Fig. 10).

XRD characterization of palladium targets

XRD spectra were collected on a Rigaku SmartLab X-ray diffractometer with Cu Kα radiation (1.5406 Å). A 2θ-omega scan for 20–90° with a scan speed of 5° min^{-1} and a step size of 0.05° was performed using parallel beam optics. The XRD spectra of the Pd targets were collected at three different stages of the experiment: (1) before a fusion experiment; (2) after a fusion experiment; and (3) after annealing the target to remove deuterium from the palladium lattice. For each stage, XRD spectra were measured on both sides of Pd targets: the side exposed to the electrolyte in the electrochemical cell and the other exposed to the D^+ beam in the vacuum chamber. Before a fusion experiment, the Pd targets were scanned after the preparation method described above. After a fusion experiment, the Pd targets were removed from the Thunderbird Reactor and transferred to the XRD in ambient air within 20 min for scanning. The Pd targets were scanned again after they were subsequently annealed at 400 °C for 1 h at 10^{-5} torr to remove deuterium from the Pd lattice.

Typical XRD spectra of Pd targets are shown in Supplementary Fig. 10. In this example, the fusion experiment included beam-loading for 60 min with a sheath voltage of −30 kV and a plasma current of 0.5 mA. This was followed by electrochemical loading for 60 min with a constant current of 200 mA across the electrochemical cell. Before fusion, the Pd target exhibited diffraction peaks for α-Pd (D/Pd < 0.01 (ref. 52)) phase on both the electrochemical cell and the beam side. The lattice constants for the α-Pd phase before fusion were determined by Bragg's law for (111), (200), (220) and (311) peaks to be 3.894 ± 0.001 Å for the electrochemical cell side and 3.8941 ± 0.0006 Å for the beam side. These values are consistent with the value of 3.889 Å of pure palladium[53]. After fusion, the Pd target exhibited diffraction peaks for α-Pd and β-Pd (D/Pd > 0.6 (ref. 52)) on the electrochemical cell side and α-Pd on the beam side. Although we speculate that the absence of β-Pd on the beam side is attributed to the instability of deuterium in the Pd lattice at high temperature caused by the ion bombardment, we do not at present have the infrastructure to provide direct evidence through in situ characterization of the Pd target in a beam-loading environment. The lattice constant of the α-Pd phase on the beam side was 3.896 ± 0.003 Å. After annealing, the Pd target exhibited α-Pd on both the electrochemical cell and beam sides, identical to the Pd target before the fusion experiment. The lattice constants for α-Pd after annealing were 3.8896 ± 0.0004 Å for the electrochemical side and 3.8925 ± 0.0004 Å for the beam side.

In situ XRD characterization of palladium targets

In situ XRD spectra were collected on a Rigaku SmartLab X-ray diffractometer with Cu Kα radiation (1.5406 Å) while the electrochemical cell was turned on. Two types of custom 3D-printed electrochemical cell fitted for in situ XRD measurements were used on the sample stage of the X-ray diffractometer. One cell exposed one side of the Pd target to ambient air while electrochemically loading the other side of the Pd target (Supplementary Fig. 11). The other cell exposed one side of the Pd target to vacuum throughout the experiment while electrochemically loading the other side of the Pd target (Supplementary Fig. 12). These cells were designed in-house using SolidWorks computer-aided design (CAD) software and 3D-printed using

a Formlabs Form 3 stereolithography 3D printer with Formlabs clear resin (urethane dimethacrylate, methacrylate monomer and photoinitiator). The 200-mA constant current between the Pd target cathode and iridium wire anode was supplied by B&K Precision model 1550 switching DC bench power supply. All in situ XRD experiments were performed at room temperature (25 °C) with a 2 M K_2CO_3 solution in H_2O as an electrolyte.

We chose the Pd(H) (111) and (200) peaks located at $2\theta = 40.1°$ and 46.6° for in situ XRD measurements. We performed looped scans from 35° to 50° with a scan speed of 5° min^{-1} and a step size of 0.05°. For the electrochemical loading cycle, the DC power supply and XRD looped scans were initiated at the same time. The DC power supply was kept on at 200 mA for 60 min to load the Pd target, during which 17 scans of XRD measurements were performed. The voltage during the loading was approximately 12 V.

After the electrochemical loading cycle, we subsequently performed either a natural outgassing cycle in ambient air or under vacuum (10^{-2} torr). To start the natural outgassing cycle, the DC power supply was turned off to keep the Pd target at its open-circuit potential, while XRD looped scans were continuously performed for 18 h.

In situ XRD spectra clearly showed the transition from α-Pd to β-Pd phase during the electrochemical loading (Extended Data Fig. 3), which occurred about 20 min after turning on the electrochemical cell. The resulting lattice constant of a β-Pd phase gives the H/Pd ratio using equation (1) in ref. 27, which is correlated to the D/Pd ratio of the Pd target in the Thunderbird Reactor. The electrochemical loading of more than 30 min yielded a single β-Pd phase. The H/Pd ratio achieved was typically around 0.7, indicating the formation of PdD with a high D/Pd ratio during the electrochemical loading in the Thunderbird Reactor.

We chose 200 mA as the current because it equates to a current density of 133 mA cm^{-2}, as we have previously reported that 100–150 mA cm^{-2} is an optimal current density in our membrane reactor[54,55]. XRD measurements of a Pd target loaded at 50 mA (Extended Data Fig. 4) indicated that the α to β transformation was too slow for the timescale of our experiments. The subsequent natural outgassing and vacuum cycles revealed that the β-Pd phase formed during the electrochemical loading cycle persisted over 18 h, both in ambient air and in vacuum (Extended Data Figs. 5 and 6). The outgassing rate did not show a notable difference between ambient air and under vacuum. The H/Pd ratio calculated from the lattice constant of the β-Pd(111) peak for the initial 60 min of the natural outgassing and vacuum cycle was higher than 0.6 for both cases, indicating that a β-Pd phase with a high H/Pd ratio was stable over the timescale of our fusion experiments with electrochemical loading cycled on and off.

Data availability

The data supporting the findings of this study are available in the paper and its Supplementary Information files. CAD files associated with this study are available at https://doi.org/10.5281/zenodo.13830012 (ref. 56).

Code availability

All code for data cleaning and analysis associated with this study are available at https://doi.org/10.5281/zenodo.13830012 (ref. 56). All code folders contain a detailed readme file to explain their use.

50. CAEN - Tools for Discovery. CoMPASS. *CAEN* https://www.caen.it/products/compass/ (2017).
51. Candler, R. N. et al. Long-term and accelerated life testing of a novel single-wafer vacuum encapsulation for MEMS resonators. *J. Microelectromech. Syst.* **15**, 1446–1456 (2006).
52. Santandrea, R. P. & Behrens, R. G. A review of the thermodynamics and phase relationships in the palladium-hydrogen, palladium-deuterium and palladium-tritium systems. *High Temp. Mater. Process.* **7**, 149–170 (1986).
53. Lässer, R. Isotope dependence of phase boundaries in the PdH, PdD, and PdT systems. *J. Phys. Chem. Solids* **46**, 33–37 (1985).
54. Stankovic, M. D. et al. Electrochemical production of methyltetrahydrofuran, a biofuel for diesel engines. *Energy Environ. Sci.* **16**, 3453–3461 (2023).
55. Stankovic, M. D., LeSage, N. E., Sperryn, J. F., Kurimoto, A. & Berlinguette, C. P. Electrochemical hydrogenation of a liquid organic hydrogen carrier using a Pd membrane reactor. *ACS Energy Lett.* **9**, 4459–4464 (2024).
56. Chen, K.-Y. Electrochemically-enhanced nuclear fusion of deuterium. *Zenodo* https://doi.org/10.5281/zenodo.13830012 (2025).

Acknowledgements This project was supported by the Thistledown Foundation, Natural Sciences and Engineering Research Council of Canada (RGPIN-2018-06748), Canada Foundation for Innovation (229288) and Canadian Institute for Advanced Research (BSE-BERL-162173). S.H. is supported by the Japan Society for the Promotion of Science Overseas Research Fellowships. T.S. acknowledges support from ARPA-E for work conducted at Lawrence Berkeley National Laboratory under DOE contract DE-AC0205CH11231. We gratefully acknowledge M. D. Trevithick, Y.-M. Chiang, J. N. Munday, D. K. Fork and R. Koningstein for helpful discussions around reactor design and A. Jalil, A. Madokoro, A. Noble, C. Waizenegger, D. Pan and M. Stankovic for technical assistance. Our sincere thanks go to past and present members of the Berlinguette Group, whose support has helped sustain this project over the years. We specifically acknowledge M. Abbas, A. Burdin, A. Hendricks, O. Horner, C. Hunt, B. R. Luginbuhl and M. Peterson. This work made use of software developed by members of the Geant4 Collaboration (http://cern.ch/geant4), as well as code libraries developed by the pandas development team (http://pandas.pydata.org) and the SciPy development team (http://scipy.org). The use of 'Thunderbird Reactor' is the internal designation used by our research group for this system; it is not affiliated with or endorsed by any trademarked entities.

Author contributions K-Y.C. contributed to the design and build of the Thunderbird Reactor, conducted primary experiments and contributed to conceptual design, data analysis and manuscript preparation. J.M. managed the project, contributed to drafting and revising the manuscript and contributed to the conceptual and experimental design, data analysis and interpreting results. P.A.S. contributed to the conceptual design and build of the Thunderbird Reactor. S.I. contributed to the design of the Thunderbird Reactor, set up and calibrated the neutron detection system and assisted with manuscript preparation. F.H.G. contributed to planning experiments, analysing data, interpreting results and manuscript writing. R.O. developed the reactor control system and supported data analysis. L.E. contributed to the conceptual and experimental design and data interpretation. S.H. conducted material characterizations, interpreted data and revised the manuscript. A.E.V. conducted nuclear Monte Carlo simulations (MCNP, Geant4, SRIM) and neutron detector calibration experiments and assisted in neutron detection, reactor experiments, data interpretation and manuscript preparation. Y.W. assisted with electrochemical cell measurements. J.Z.X.K. contributed to the reactor engineering design and fabrication. T.S. contributed to the experimental design. M.S. and A.K.B. contributed to project management, experiment design and manuscript writing. C.P.B. supervised the study, defined the hypotheses and designed the project.

Competing interests The authors declare no competing interests.

Additional information

Supplementary information The online version contains supplementary material available at https://doi.org/10.1038/s41586-025-09042-7.

Correspondence and requests for materials should be addressed to Curtis P. Berlinguette.

Peer review information *Nature* thanks Andreas Borgschulte, Jennifer Dionne, Thomas Fuerst and the other, anonymous, reviewer(s) for their contribution to the peer review of this work.

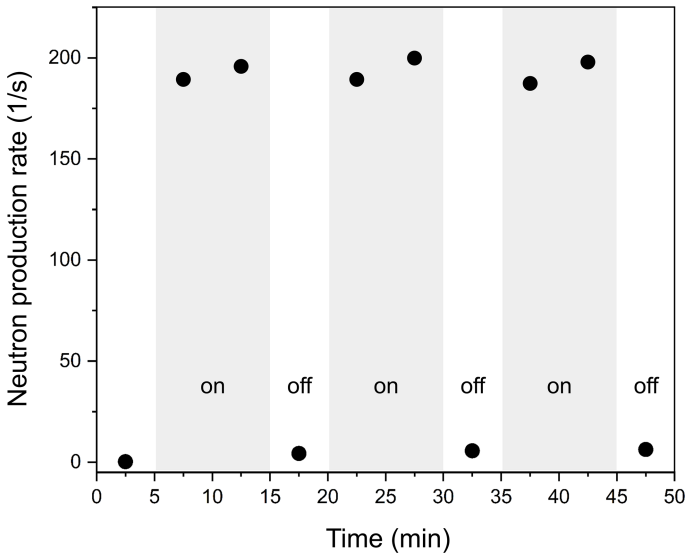

Extended Data Fig. 1 | Experimental confirmation of fusion occurring within the lattice of the metal target. Neutron production rates were observed when the sheath voltage of the reactor was cycled on and off during a beam-loading experiment. During the 10-min 'on' periods, the sheath voltage accelerated D^+ into the palladium target. During the 5-min 'off' periods, the sheath voltage was turned off, effectively stopping the D^+ ions from being implanted into the palladium target. The highest neutron production rate during this experiment was 188(2) n s^{-1}.

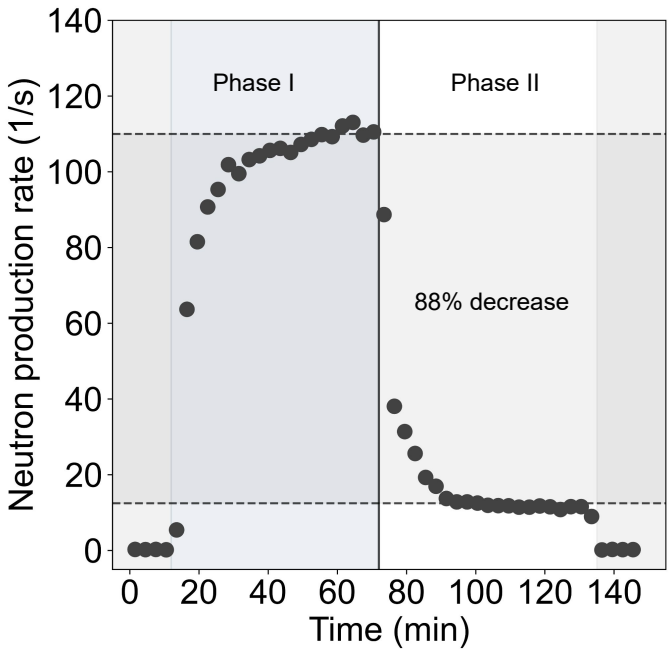

Extended Data Fig. 2 | The impact of using H_2O as a solution on neutron production rate. 2 M K_2CO_3 in H_2O was used as the electrolyte in the Thunderbird Reactor. In this case, after the electrochemical cell was activated (phase II), the neutron production rate decreased by 88.3(3)% compared with the rate observed in phase I.

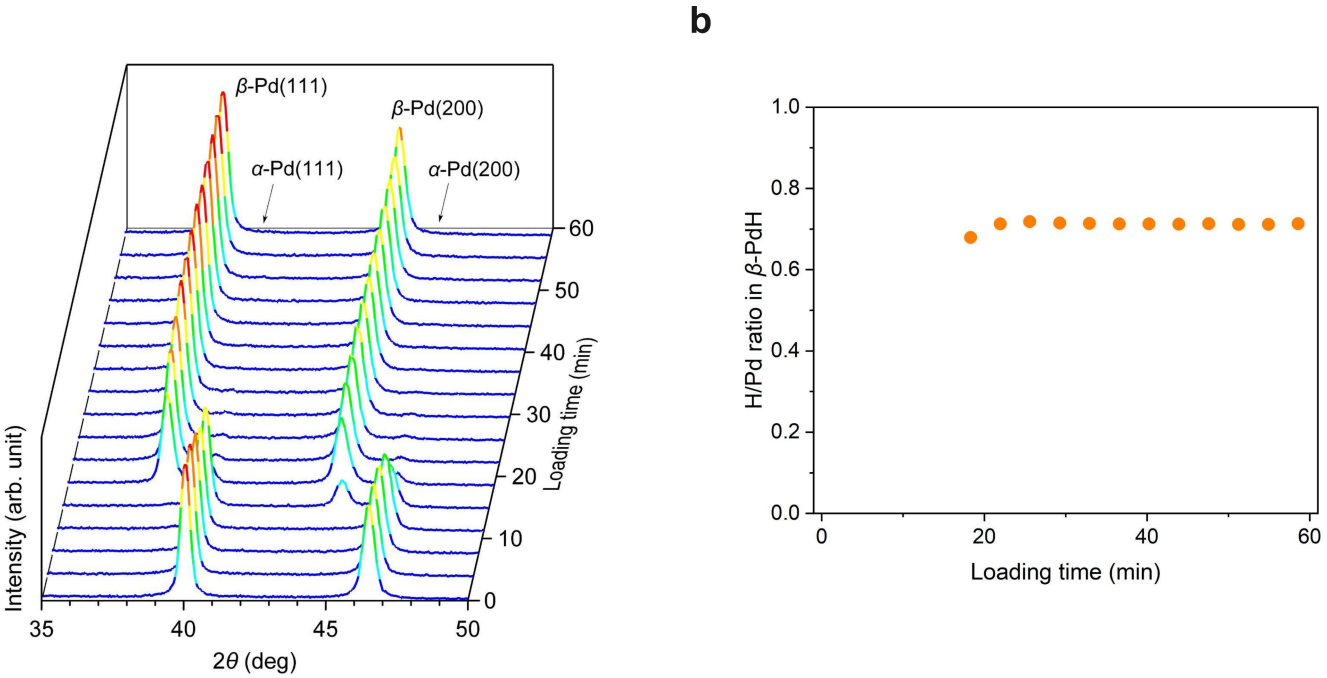

Extended Data Fig. 3 | In situ XRD experiments for electrochemical loading cycle. a, 3D perspective view of XRD patterns of a Pd target as a function of electrochemical loading time. The Pd target was electrochemically loaded with hydrogen sourced from water electrolysis in 2 M K_2CO_3 in H_2O with a constant current of 200 mA for 60 min. Throughout this duration, XRD measurements were conducted repeatedly for $2\theta = 35–50°$ at a scan rate of 5° min^{-1}. **b**, H/Pd ratio calculated from the lattice constant of the β-Pd(111) peak[27] as a function of loading time.

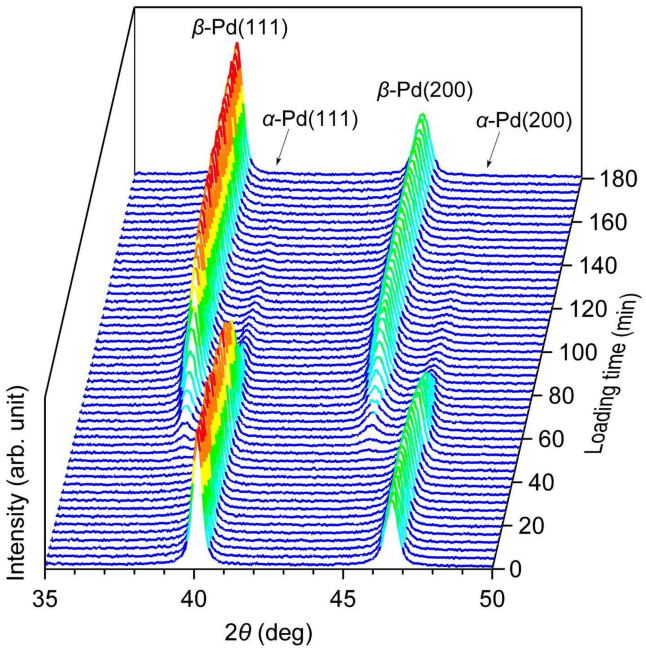

Extended Data Fig. 4 | 3D perspective view of in situ XRD patterns of a Pd target as a function of electrochemical loading time. The Pd target was electrochemically loaded with hydrogen sourced from water electrolysis in 2 M K_2CO_3 in H_2O with a constant current of 50 mA for 180 min. Throughout this duration, XRD measurements were conducted repeatedly for $2\theta = 35–50°$ at a scan rate of 5° min^{-1}.

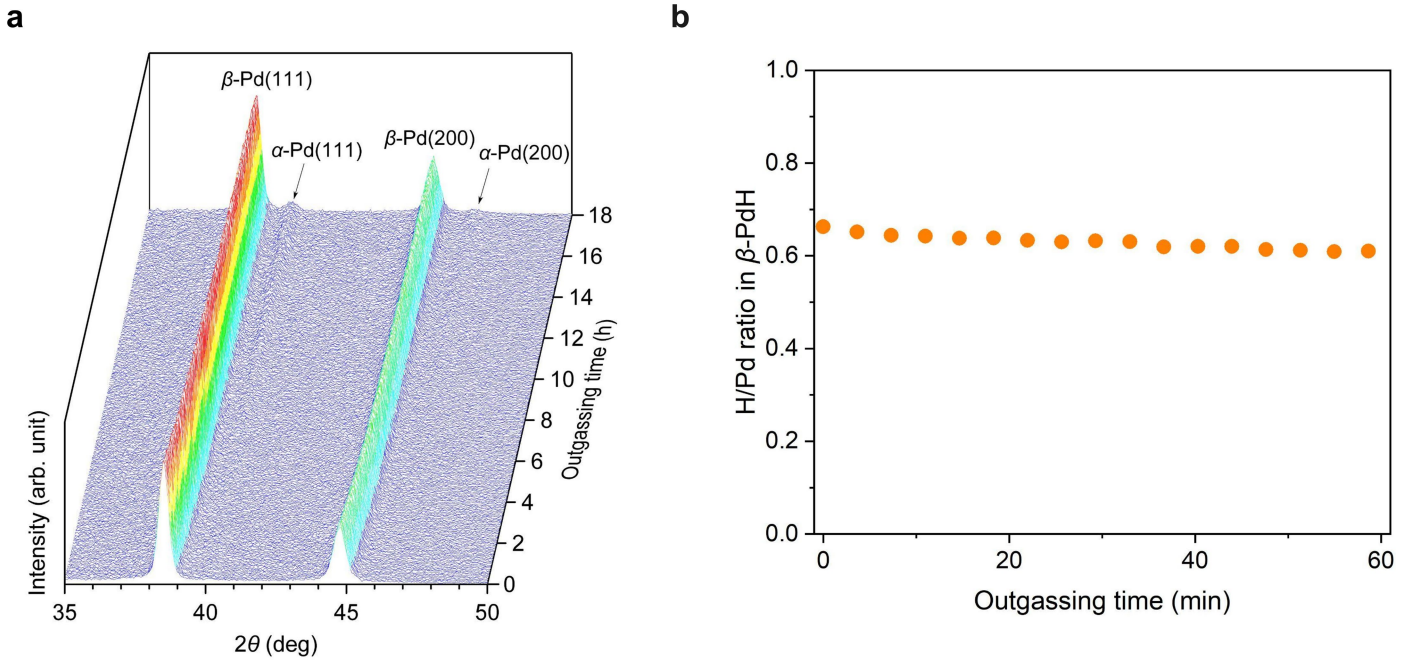

Extended Data Fig. 5 | In situ XRD experiments for a natural outgassing cycle. a, 3D perspective view of XRD patterns of a Pd target as a function of outgassing time. The Pd target was first electrochemically loaded with hydrogen sourced from water electrolysis in 2 M K_2CO_3 in H_2O at a constant current of 200 mA for 60 min and then kept at its open-circuit potential for 18 h. Throughout this duration, XRD measurements were conducted repeatedly for $2\theta = 35–50°$ at a scan rate of 5° min^{-1}. **b**, H/Pd ratio calculated from the lattice constant of the β-Pd(111) peak[27] as a function of time for the initial 60 min of the outgassing cycle.

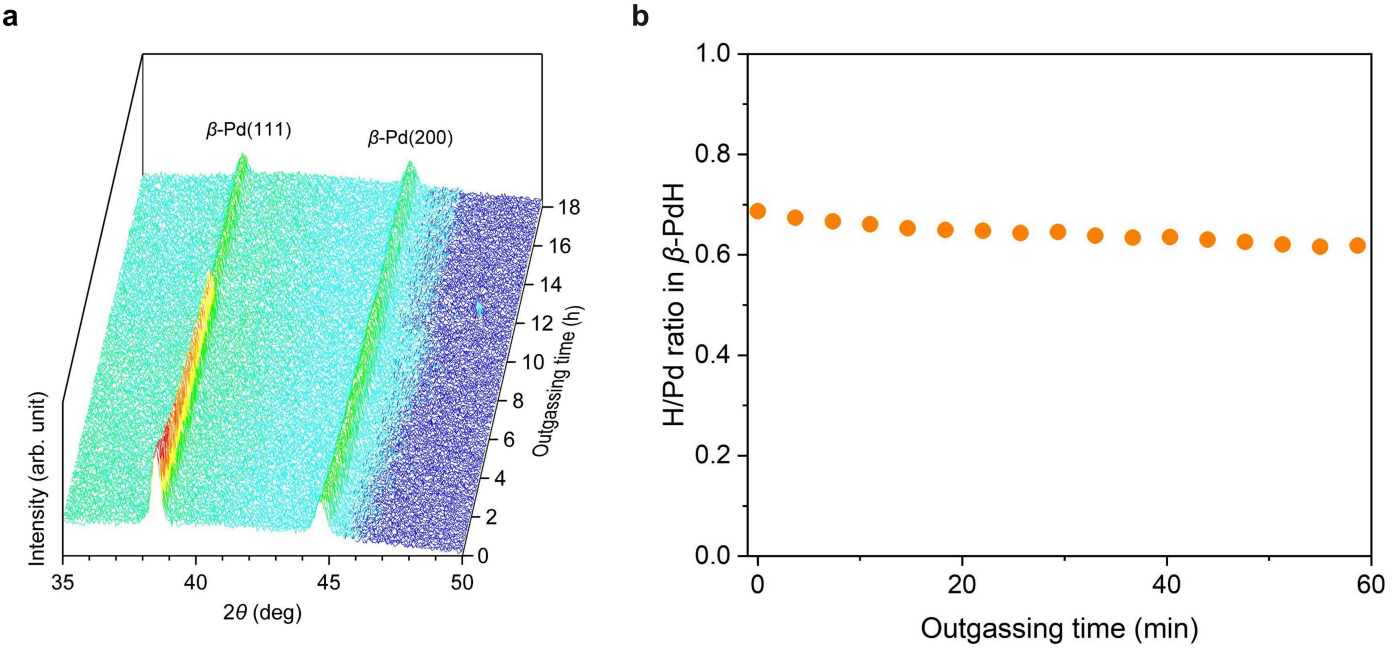

Extended Data Fig. 6 | In situ XRD experiments for a vacuum cycle. a, 3D perspective view of XRD patterns of a Pd target as a function of outgassing time. The Pd target was first electrochemically loaded with hydrogen sourced from water electrolysis in 2 M K_2CO_3 in H_2O at a constant current of 200 mA for 60 min and then kept at its open-circuit potential for 18 h. Throughout this duration, XRD measurements were conducted repeatedly for $2\theta = 35–50°$ at a scan rate of 5° min^{-1}. The cell was left under a vacuum of 1.2×10^{-2} torr. **b**, H/Pd ratio calculated from the lattice constant of the β-Pd(111) peak[27] as a function of time for the initial 60 min of the outgassing cycle.

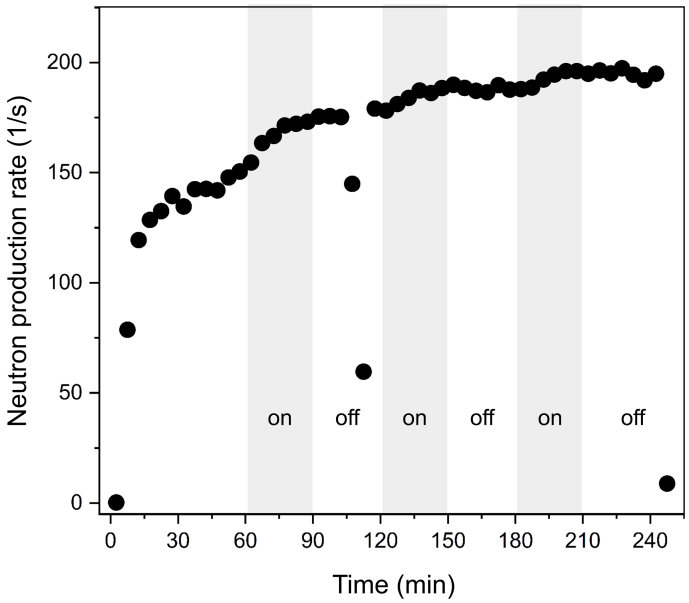

Extended Data Fig. 7 | The effect of power cycling the electrochemical cell. Neutron production rates when the electrochemical cell was cycled on and off. The first 60 min are the beam-loading period only and, after reaching saturation, the electrochemical cell on/off cycle begins. During the 30-min 'on' periods, the deuterium was electrochemically loaded into the Pd target at a current of 200 mA. During the 30-min 'off' periods, the electrochemical loading of deuterium into the Pd target was stopped. The neutron production rate increased with time while the electrochemical cell was 'on' and stopped increasing when the electrochemical cell was 'off'. Beam loading was 'on' for the duration of the entire experiment.